

**Motility induced phase separation of deformable cells**

Journal:	<i>Soft Matter</i>
Manuscript ID	SM-ART-08-2023-001059.R1
Article Type:	Paper
Date Submitted by the Author:	04-Oct-2023
Complete List of Authors:	Hopkins, Austin; University of California Santa Barbara, Physics Loewe, Benjamin; The University of Edinburgh, Physics and Astronomy Chiang, Michael; The University of Edinburgh, Physics and Astronomy Marenduzzo, Davide; The University of Edinburgh, Physics and Astronomy Marchetti, M.; University of California Santa Barbara, Physics

Cite this: DOI: 00.0000/xxxxxxxxxx

Motility induced phase separation of deformable cells[†]

Austin Hopkins^{*a}, Benjamin Loewe^{b‡}, Michael Chiang^{b‡}, Davide Marenduzzo^{b‡}, and M. Cristina Marchetti^{*a}

Received Date

Accepted Date

DOI: 00.0000/xxxxxxxxxx

Using a multi-phase field model, we examine how particle deformability, which is a proxy for cell stiffness, affects motility induced phase separation (MIPS). We show that purely repulsive deformable, i.e., squishy, cells phase separate more effectively than their rigid counterparts. This can be understood as due to the fact that deformability increases the effective duration of collisions. In addition, the dense regions become increasingly disordered as deformability increases. Our results contextualize the applicability of MIPS to biological systems and have implications for how cells in biological systems may self-organize.

1 Introduction

Self-propelled particles¹ have been used as a simple model for synthetic active swimmers and biological systems, and can describe collective phenomena such as flocking^{2–5}, aggregation^{6,7} and sorting^{8–10}. Although biological systems often have complex physical interactions, it has been shown that motility is sufficient to induce phase separation of purely repulsive particles. This phenomenon is known as motility induced phase separation (MIPS) because, unlike in equilibrium systems, the phase separation can occur without attractive interactions. MIPS has been extensively studied in the context of self-propelled repulsive spheres, known as active Brownian Particles (ABPs), and it has been described in terms of the suppression of the effective motility due to crowding^{11–18}, the kinetics and mechanics of the phase-separated interface^{19?}, and an effective attractive interaction²⁰. The phase behavior of rigid, repulsive active particles has been mapped out as a function of motility and density²¹, and the effects of other properties like polydispersity²², particle shape²³, friction between particles²⁴, and interaction softness^{25–27} have also been studied.

One shortcoming, however, is that studies have focused on rigid particles, even though the cells that make up biological systems can change their shape. Therefore, we study here a system of deformable active particles to better understand the applicability of MIPS to biological systems, or to cell suspensions. We find that, at a given density, more deformable particles are more prone to phase separate than less deformable ones. This result can be explained by an increase in the duration of two-body collisions with increasing deformability. We also find that deformability fundamentally affects the structure of the dense phase, which is crys-

talline at low deformability and becomes glassy with increasing deformability.

In the remainder of the paper we first introduce the phase field model in Section 2. The results are presented in Section 3, including the numerically evaluated phase diagram, a phenomenological argument that relates the deformability-induced enhancement of phase separation to the duration of binary collisions, and an analysis the structural properties of the dense phase. We conclude with a brief summary and outlook in Section 4.

2 Model

We model N cells as deformable particles, each described by a phase field $\phi_i(\mathbf{r})$ ^{28–37}. The phase field model allows us to describe arbitrary cell shapes and to vary the cell edge tension. Phase field models have been shown to capture many mechanical properties of tissue monolayers^{30,31,34,36,37}. The free energy of the system is

$$\mathcal{F} = \sum_{i=1}^N \left[\kappa \int d^2\mathbf{r} \left(\phi_i^2 (\phi_i - 1)^2 + \xi^2 (\nabla \phi_i)^2 \right) + \lambda \pi R^2 \left(1 - \int d^2\mathbf{r} \frac{\phi_i^2}{\pi R^2} \right)^2 + \varepsilon \sum_{i<j=1}^N \int d^2\mathbf{r} \phi_i^2 \phi_j^2 \right]. \quad (1)$$

The first term sets the field ϕ_i to be 1 in the interior of the cell and 0 in the exterior. The second term penalizes gradients in the field with a stiffness proportional to κ . The third term sets the preferred cell area to that of a circle of radius R . An isolated cell will be circular, as in Fig. 1 (a). The resulting ϕ_i profile interpolates from 0 outside the cell to 1 inside the cell, as in Fig. 1 (b), with interfacial thickness ξ . The last term incorporates steric repulsion by penalizing overlap between different cells with strength ε . When two cells interact, they may overlap or they may change their shape to avoid overlapping. We define the deformability d

^a Department of Physics, University of California Santa Barbara, Santa Barbara, CA 93106, USA. E-mail: xxx@aaa.bbb.ccc

^b School of Physics and Astronomy, University of Edinburgh, Peter Guthrie Tait Road, Edinburgh EH9 3FD, United Kingdom.

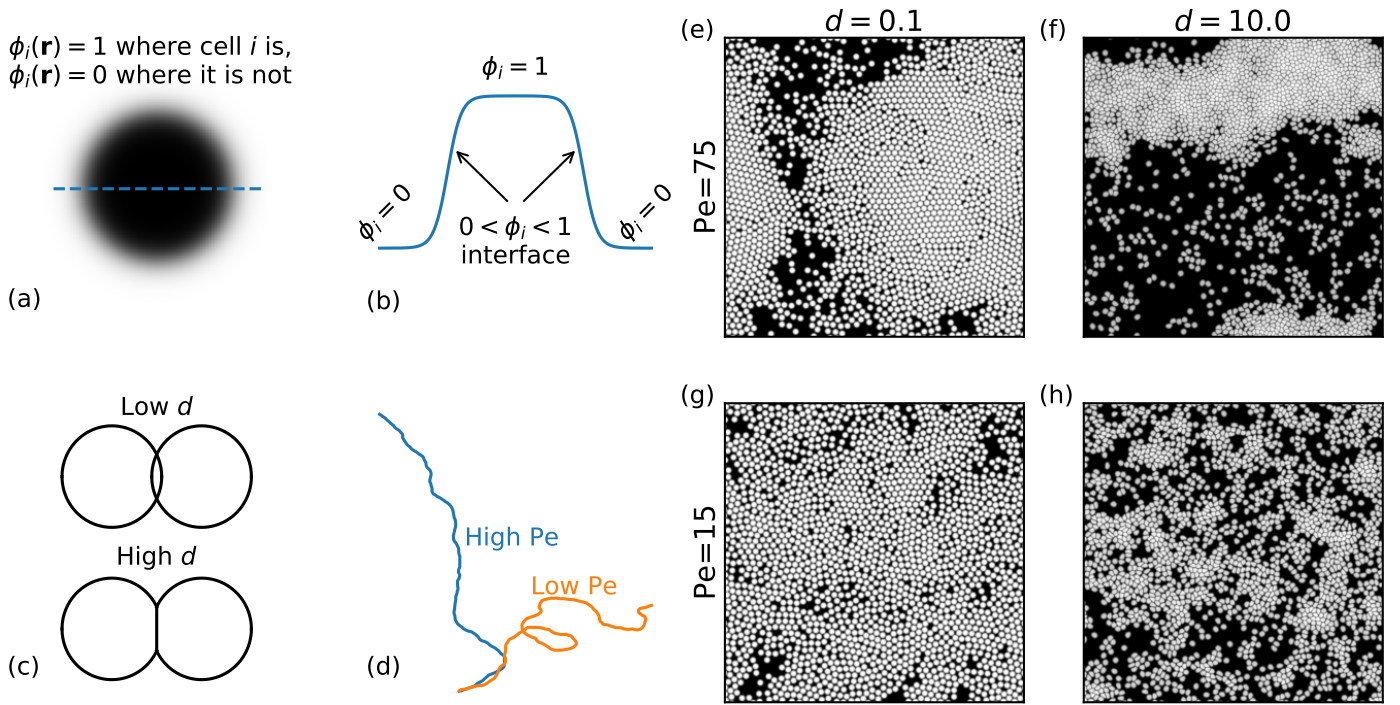


Fig. 1 Illustrations of the model features (a)-(d) along with snapshots of the particles in the full simulations (e)-(h). (a) shows an isolated cell, which is circular. (b) shows a typical profile for the phase field of a cell. (c) depicts how cells at a low d will tend to overlap while maintaining a circular shape, while at a high d cells will change shape to avoid overlapping. (d) illustrates sample trajectories for isolated cells whose Pe differs by a factor of 5. The snapshots in (e)-(h) show the full system at low and high d and Pe as indicated.

as the ratio of the characteristic energy of overlap to the characteristic energy of shape deformation: $d = \frac{1}{12}(\varepsilon\xi R)/(\sigma R) = \frac{\varepsilon}{4\kappa}$. $\sigma = \kappa\xi/3$ is the cell-edge tension and the factor of $\frac{1}{24}$ brings this definition in line with previous work³², in which $d \sim 1$ was shown to result in a qualitative change in the cellular interactions. Figure 1 (c) qualitatively illustrates how varying d changes the interactions between cells. We also define the cell compressibility $\chi = \lambda/\varepsilon$, which we keep fixed at $\chi = 50$. This value of the compressibility allows for polydispersity while preventing cells from collapsing.

We model cells crawling on a substrate, which leads to the following evolution equation for the fields

$$\frac{\partial \phi_i}{\partial t} + \mathbf{v}_i \cdot \nabla \phi_i = -\frac{1}{\gamma} \frac{\delta \mathcal{F}}{\delta \phi_i}, \quad (2)$$

where γ is the inverse mobility. We incorporate the cell motility via the advection term in the field equation. The advection velocity is determined by self-propulsion and interaction terms arising from passive forces, which arise from the gradients of the chemical potential³⁸,

$$\mathbf{v}_i = v_0 \hat{\mathbf{p}}_i + \frac{1}{\Gamma A_i} \mathbf{f}_i, \quad (3)$$

where $\hat{\mathbf{p}}_i = (\cos \theta_i, \sin \theta_i)$ is the cell polarity which determines the direction of isolated cell motion. The passive forces are given by

$$\mathbf{f}_i = -\sum_j \int d^2 \mathbf{r} \phi_i \phi_j \nabla \mu_j, \quad (4)$$

with $\mu_j = \frac{\delta \mathcal{F}}{\delta \phi_j}$ the chemical potential of cell j , $A_j = \int d^2 \mathbf{r} \phi_j^2$ the cell's area, and Γ a friction per unit area. We assume that all cells have the same self-propulsion speed v_0 . The direction θ_i diffuses at a rate D_r , i.e., $d\theta_i(t) = \sqrt{2D_r} dW_i(t)$, where $dW_i(t)$ is a Wiener process. We quantify the activity via the Péclet number $Pe = v_0/(RD_r)$, which is the ratio of the cell's persistence length $\ell_p = v_0/D_r$ to its size. The effect of varying Pe on cell trajectories is illustrated in Fig. 1 (d).

In the following we take R as our unit of length, R/v_0 as unit of time, and εR^2 as unit of energy. In these units $v_0 = 1$ and we fix the interfacial thickness $\xi = 1/8$. Our equation then contain a dimensionless substrate friction per unit area $\tilde{\Gamma} = \Gamma R v_0 / \varepsilon$ and a dimensionless inverse mobility $\tilde{\gamma} = \gamma v_0 / (\varepsilon R)$. In the following all quantities are dimensionless and we drop the tilde. All results are for $\tilde{\Gamma} = 4.375 \times 10^{-2}$ and $\tilde{\gamma} = 4.375 \times 10^{-2}$. The model parameters and their values are summarized in table 1.

3 Phase separation of deformable particles

To study motility-induced phase separation, we simulate 2,000 cells in a square simulation box of length $L = 112.125$, giving a packing fraction $\phi = \frac{N\pi R^2}{L^2} = 0.5$. At fixed packing fraction, we vary both d and Pe . We vary Pe by varying D_r (see Table 1). Since we work at a fixed interfacial thickness ξ , we vary d by changing the cell edge tension σ . We show snapshots from several of these simulations in Fig. 1 (e)-(h). At low Pe the system does not phase separate regardless of the value of d . Fig. 1 (g,h). As Pe is increased, phase separation occurs for both values of d Fig. 1 (e,f). One qualitative difference is that the dense phase in the

high d system takes up less area because the deformable cells can pack closely, while the rigid disk-like cells in the low d system cannot pack as tightly.

3.1 Deformability enhances phase separation

We find that, like in studies on rigid particles, phase separation occurs above a critical Pe . To quantify the onset of phase separation we divide the system into square subsystems of size $10R$ and calculate the local density ρ_L , defined as the area fraction of the subsystem where the local phase field is greater than 0.5. Examples of the distributions of ρ_L are shown on the left side of Fig. 2. This particular definition of the local density captures the fraction of the area that is excluded by steric interactions. It also allows the most accurate comparison between low and high d systems because the values are restricted between 0 and 1, even if the fields in tightly compressed cells reach values above 1. We have verified that varying the subsystem size does not qualitatively change the distributions, as long as the subsystem size remains significantly larger than R but smaller than L . When the system phase separates, the local density distribution changes from unimodal to bimodal. To quantify this change we use the variance of the distribution and choose a cutoff of 0.0378 to identify phase separation. The resulting phase diagram is shown on the right side of Fig. 2, where the variances have been normalized by this cutoff. As one can see from the histograms on the left side of Fig. 2, the chosen cutoff separates the homogeneous and phase separated systems. The required Pe for phase separation decreases with increasing d .

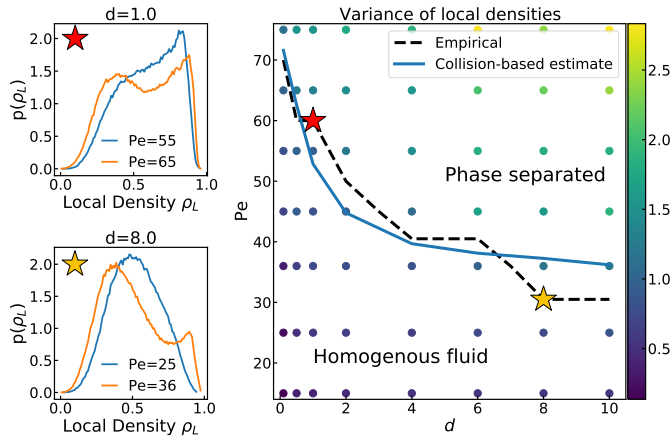


Fig. 2 Left: local density curves for two different d , showing the difference in the distribution below and above the empirically determined cutoff. Right: phase diagram based on the variance of the local density distributions, with a fit based on the deformability dependence of the duration of two-body collisions. The stars indicate the deformabilities corresponding to the distributions on the left. The variance is normalized by the empirically chosen cutoff for phase separation.

3.2 Deformability modifies the effective duration of a collision

Previous work on motility-induced phase separation has shown that the transition from a homogeneous fluid to a phase separated state can be captured by continuum models formulated in

terms of coarsened grained density and polarity fields.^{12,14–16} Interactions renormalize the self-propulsion speed v_0 , which becomes $v(\rho)$, a function of the density. To capture the deformability dependence of the phase diagram, we start from the observation that at long times an isolated ABP behaves as a random walk of step length $\ell_p \simeq v_0 \tau_p$, with $\tau_p = D_r^{-1}$. Following the argument given in Ref.¹⁵, we note that an ABP will be slowed down by collisions during each step of length ℓ_p , resulting in a reduction of the effective step length $\ell(\rho) < \ell_p$. Denoting by n_c the number of collisions in τ_p , and by τ_s the typical stalling time associated with each collision, the effective step length can be written as $\ell(\rho) = v_0(\tau_p - n_c \tau_s)$. The effective self-propulsion speed is then given by $v(\rho) = \ell(\rho)/\tau_p$. We estimate the number of collisions in a time τ_p as $n_c \simeq \tau_p/\tau_{\text{mft}}$, where τ_{mft} is the mean free time between collisions. This is controlled by the scattering cross section and for circular particles can be written in terms of the number density ρ as $\tau_{\text{mft}} = 1/(2Rv_0\rho)$. The effective propulsive speed can then be written as¹⁶

$$v(\rho) \simeq v_0 \left(1 - \frac{\tau_s}{\tau_{\text{mft}}} \right). \quad (5)$$

This derivation makes sense at low densities, where $\tau_{\text{mft}} \gg \tau_s$, and two body collisions are the primary cause of velocity slow-down. Eq. (5) predicts a linear dependence of velocity on density. This has been observed empirically to hold to a good approximation up to much larger densities which might be *a priori* expected on the basis of this simple derivation¹⁵.

Previous work^{12,14–16} on continuum models of MIPS has shown that the onset of phase separation can be understood qualitatively by a linear instability associated with the vanishing of an effective diffusion coefficient, given by¹⁶

$$\mathcal{D}(\rho) = \frac{v^2(\rho)}{2D_r} \left(1 + \frac{d \ln v(\rho)}{d \ln \rho} \right). \quad (6)$$

Within our approximation in Eq. (5), MIPS ensues when $\tau_s \sim \tau_{\text{mft}}$, which is also when such an approximation breaks down, suggesting that many-body collisions become important.

To estimate the stalling time τ_s , and hence the onset of MIPS in our deformable droplet system, we note that the latter is mainly controlled by two processes: the reorientation that occurs at rate D_r and the fact that collisions among deformable particles have a finite duration τ_c . Assuming that τ_s is controlled by the faster of these two processes, we write $\tau_s^{-1} = a_1 D_r + a_2 \tau_c^{-1}$, with a_1 and a_2 fitting parameters expected to be of order one. We then estimate the deformability dependence of τ_c , i.e., the time it takes for particles to move past one another due to interactions, by examining numerically two body simulations of nearly head-on collisions in the limit $D_r = 0$, where particles cannot escape the collision by turning their nose. We find that τ_c depends strongly on deformability (Fig. 3). Using this estimate in the instability condition $\tau_{\text{mft}}(\rho) = \tau_s(d)$ we obtain the dashed line in Fig. 2, with $a_1 = 3.70$ and $a_2 = 1.42$. Therefore we find that the criterion $\tau_s = \tau_{\text{mft}}$ predicts well the onset of MIPS, so that the strong dependence of the stalling time on deformability obtained from two body collisions captures the increasing propensity of more deformable particles

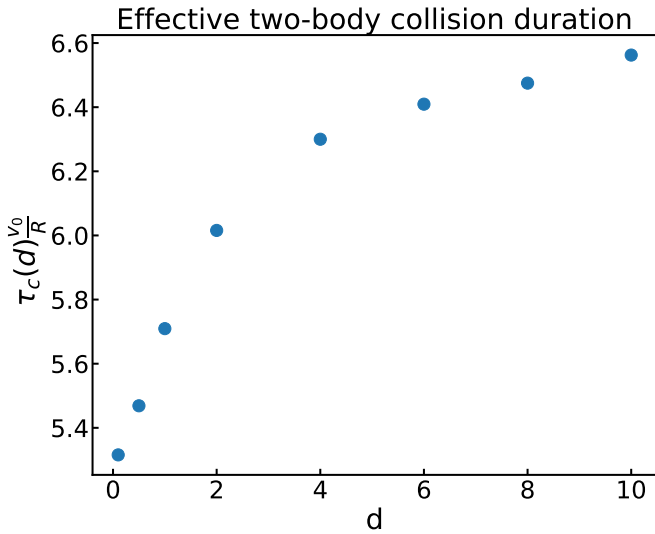


Fig. 3 The collision duration τ_c as measured from two body simulations of nearly head-on collisions with $D_r = 0$ increases with increasing particle deformability. See Appendix B for more details.

to phase separate.

3.3 Structure of the dense phase

The dense phase becomes more disordered as deformability increases. This is evident from Fig. 4(a) and (b), where we show snapshots in which the cells are colored by their number of neighbors as determined by a Voronoi construction of their centers of mass. Clearly the number of structural defects increases with deformability. To quantify the structure, we define the bond-orientational order of a cell j as $\Psi_{6,j} = \frac{1}{N_{nn,i}} \sum_{k \in nn} e^{i6\theta_{j,k}}$, where the sum is over the k nearest neighbors and $\theta_{j,k}$ is the angle between the center of mass of cell j and cell k . We define the local bond-orientational order $|\Psi_6|_{loc}$ as the average of $\Psi_{6,j}$ over the cells within a subsystem of size $10R$. We show the distributions of this quantity in Fig. 4, for low (c) and high (d) deformability. At low deformability the distribution has a peak near $|\Psi_6|_{loc} \sim 1$, corresponding to local hexatic order of the dense clusters, and a second peak at a small values of $|\Psi_6|_{loc}$ arising from the disordered low density gas. For high deformability, however, there is no local hexatic order in the dense clusters, and the distribution has a single peak at low $|\Psi_6|_{loc}$. The increase in disorder as a function of deformability is similar to the change seen in the confluent deformable particle monolayer studied in previous work.³⁵

4 Summary

In summary, we have characterized numerically the phase diagram of a system of purely repulsive deformable active particles as a function of their deformability and motility. This case is an important one to consider when the applicability of motility-induced phase separation to biological systems, such as cell suspensions, is considered: indeed, cells behave differently from colloidal rigid particles, and can be better represented by deformable droplets.

We have shown that, like rigid APBs, deformable particles

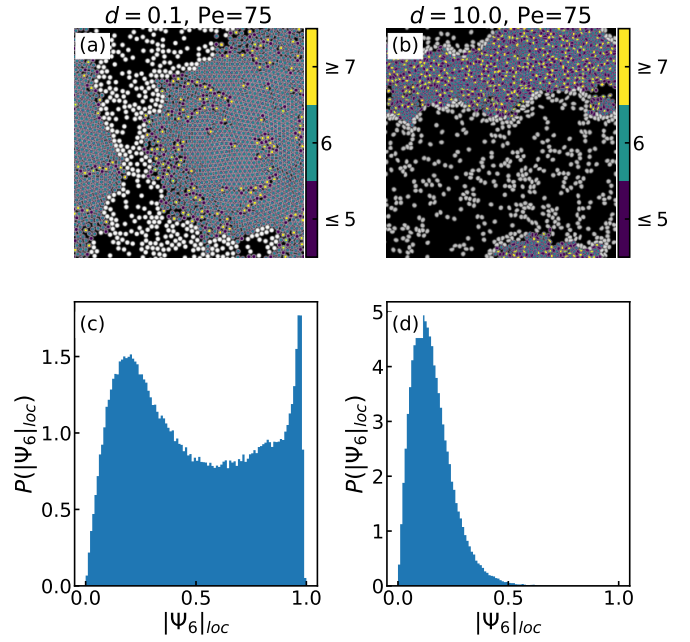


Fig. 4 Top row: snapshots of the phase-separated system with some of the particles in the dense phase colored by the number of neighbors as determined by a Voronoi diagram of the centers of mass for low ((a), $d = 0.1$) and high ((b), $d = 10$) deformability. Bottom row: corresponding (time-averaged) distributions of the local bond-orientational order parameter $|\Phi_6|_{loc}$.

phase separate into a dilute and dense phase for sufficiently persistent motility. However, we found that deformability has two important effects on motility-induced phase separation. First, deformable particles are able to phase separate at a significantly lower motility than rigid ones. This effect can be explained by the fact that deformability increases the duration of two-body collisions, thereby enhancing the slow-down of motility induced by crowding. Second, deformability strongly affects the nature of the high-density phase, which is glassy for squishy (more deformable) particles, which become polydisperse, and near-crystalline for rigid (less deformable) particles. It would be of interest to study in the future the dynamics within the high-density phase, to assess whether the structural differences we have observed translate into a dynamical phase transition between the two regimes.

We stress that increasing deformability in our work has a distinctly different effect from the softening of the repulsive interaction. Previous work on simulations of rigid repulsive APBs has shown that softening the repulsive interaction suppresses both motility-induced phase separation and bond orientational order²⁵. Phase separation in that context is suppressed because softer repulsive interactions allow particles to overlap, which reduces the amount that particles are slowed down due to collisions. In contrast, deformability, as implemented in our work, suppresses overlap and enhances the slow down due to collisions, which promotes phase separation.

Future work will be needed to further connect MIPS to biological systems. Additional interactions beyond steric repulsion, such as differential adhesion³⁹, as well as chemically mediated

interactions^{40,41}, may enhance cell aggregation or affect pattern formation in real systems. A further interesting generalization would be to consider mixtures of deformable and rigid particles, which could lead to sorting between cells within the high-density phase.

Author Contributions

Conceptualization: A.H., B.L. and M.C.M.; Data curation: A.H. and B.L.; Formal analysis: A.H. and B.L.; Funding acquisition: M.C.M. and D.M.; Investigation: A.H. and B.L.; Methodology: all; Software: A.H., B.L., and M.C.; Supervision: M.C.M.; Visualization: A.H. and B.L.; Writing - original draft: A.H.; Writing - review & editing: all

Conflicts of interest

There are no conflicts to declare.

Appendix A Role of interaction forces in the advection equation

Phase field models used in previous literature have either included^{30,31} or neglected^{32,37} the passive interaction forces in Eq. 3 for the cell advection velocity. These interaction forces arise from cellular stresses when the 3D force balance equation is averaged over the cell thickness to obtain a 2D model of cells coupled to a substrate.⁴² We show here that the presence/absence of these forces has a significant effect on MIPS. Specifically, the effect of deformability on MIPS is reversed when the passive interaction forces are not included in the force balance equation for the advection of velocity. In this case, increasing deformability suppresses rather than enhances phase separation even at high motility. To understand this we recall that MIPS occurs when crowding suppresses motility. For rigid particles with purely repulsive interactions the reduction of the motility of particle i is given by the component of the repulsive force on that particle along its direction of self propulsion and can be estimated to linear order in density, as shown in Ref.¹⁴. When passive forces are neglected in the force balance equation, there are simply no interactions that can renormalize the motility. Increasing deformability then allows cells to more easily squeeze through their neighbors, slightly increasing the particles' effective motility (Fig. 5(b)) and suppressing MIPS. This effect can also be observed by visually inspecting the phase separated system (see Fig. 5(c)): passive forces help cells keep away from each other, leading to larger clusters. In their absence, the same deformability and motility lead to sparser clusters.

To demonstrate the effect of the passive forces on the effective velocity v_i of a cell, we have performed simulations of the head-on collision dynamics of two particles at various values of the substrate friction Γ . It is clear from the force balance equation, Eq. 3, that increasing Γ reduces the importance of the passive forces, which eventually drop out entirely for $\Gamma \rightarrow \infty$, where $v_i \approx v_0 \hat{p}_i$. We show in Fig. 6 the duration of a binary collision as a function of deformability for various values of Γ . It is evident that while at small Γ the duration of collision increases with deformability, as shown in the main text, this behavior is reversed

at high Γ , where the collision is only indirectly slowed down by shape changes in the evolution of the phase fields, Eq. 2. In this case more deformable particles can squeeze more easily around the obstacle provided by another particle. The small nonmonotonic region at intermediate Γ (green dots in Fig. 6) and small deformability is due to the competing effects of the particle shape changes and passive forces on the collision duration. Initially, the shape changes allow the particles to move past one another more quickly. However, as deformability increases further, the shape changes result in greater passive forces along the direction of the collision, thus slowing the particles down.

Appendix B Details of two-body collisions

We consider two particles, initially isolated and circular, which propel towards each other in a head-on collision. All the cell parameters are as in the main text, except $D_r = 0$ to eliminate rotational noise. We offset the particles by one lattice point (impact parameter $b = \frac{1}{8}R$) so that they are nearly head-on, but are still able to move past one another in the absence of noise. We focus on nearly head-on collisions because those are the ones which significantly slow down a particle, and hence are the most important for cluster formation. We choose a cutoff of $\phi_1 + \phi_2 = 0.1$ to define when the two particles are in contact with one another, and measure the collision duration as the total time the particles are in contact. As can be seen in Fig. 7, when particles with high d collide (bottom row), their shape changes, which slows their motion past one another.

Appendix C Table of Parameters and Simulation Details

Table 1 Value(s) of the parameters used in the simulations.

Parameter	Interpretation	Dimensions	Value(s)
d	deformability	-	0.1 – 10
R	cell radius	[L]	1
ξ	cell interface thickness	[L]	1/4
ϵ	strength of repulsion	[E] [L] ⁻²	1
χ	cell compressibility	-	50
γ	inverse mobility	[E][T][L] ⁻²	4.375×10^{-2}
Γ	substrate friction density	[E][T][L] ⁻⁴	4.375×10^{-2}
v_0	cell self-propulsion speed	[L][T] ⁻¹	1
D_r	polarity diffusion rate	[T] ⁻¹	1/75 – 1/15
dt	time step	[T]	2.1875×10^{-4}
dx	lattice size	[L]	1/8
L_{sub}	cell subdomain size	[L]	4.375
L	simulation box size	[L]	112.125
ϕ	packing fraction	-	0.5

We have chosen the preferred cell radius as unit of length ($R = 1$), R/v_0 as unit of time ($v_0 = 1$), and the repulsion strength over cell area as unit of energy ($\epsilon R^2 = 1$). To compare with a physical system of cells, we can match the cell radius and self-propulsion speed to the data for isolated cells in Table 1 of Ref.⁹ for keratocytes. This results in a radius $R \sim 10 \mu\text{m}$, and $v_0 \sim 558 \mu\text{m/hr}$.

We simulate Eq. (2) using finite differences, and a 3rd order upwind scheme for the advection velocity. The simulation lattice spacing is $dx \sim 1.25 \mu\text{m}$ with a total box size $L \sim 0.1 \text{cm}$ and the

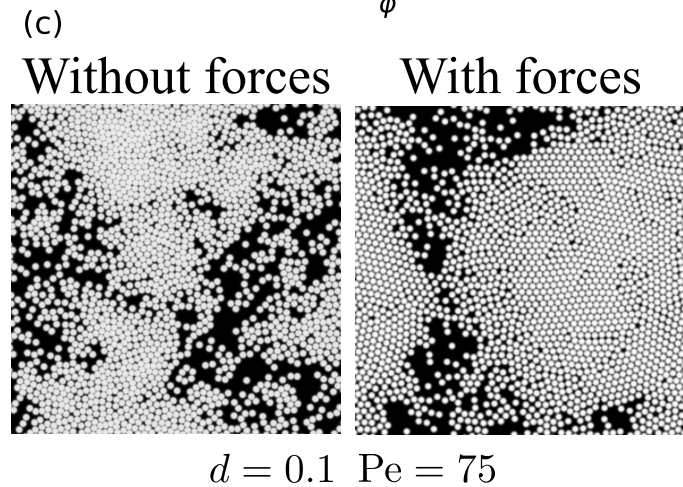
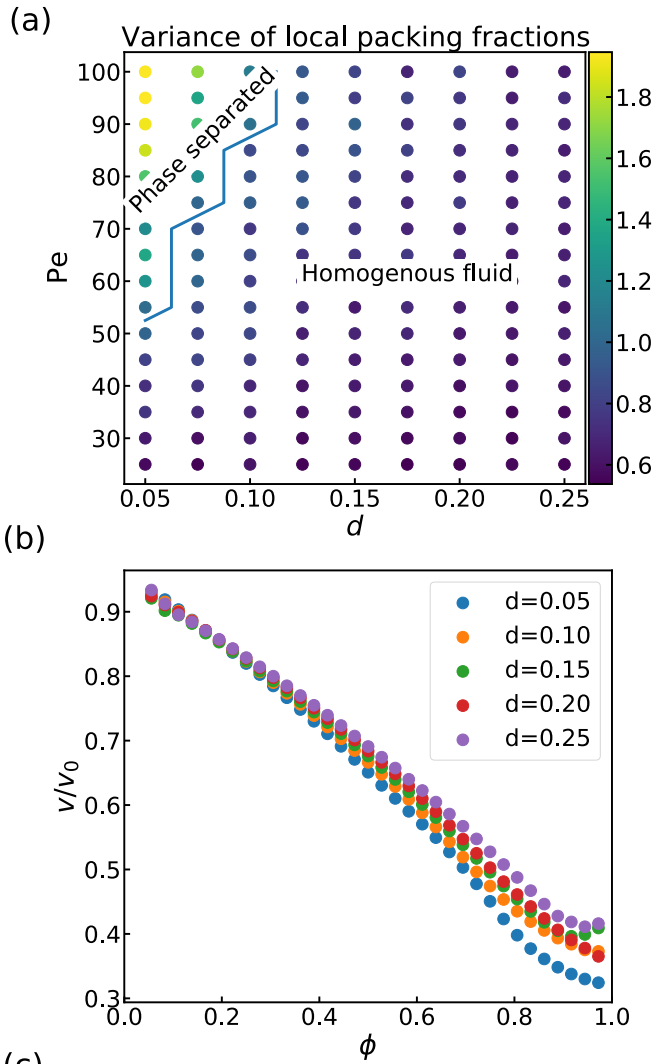


Fig. 5 (a) Phase diagram obtained simulations using the model of Ref. ³² without passive forces in Eq. (3). Colorbar: variance of the local packing fraction, normalized by a cutoff 0.0252, which corresponds to the difference between a unimodal and bimodal distribution in this model. In the absence of passive forces, deformability suppresses phase separation. (b) Cell velocity as a function of local packing fraction for cells without passive forces. Increasing deformability reduces the slow-down induced by crowding, thus suppressing MIPS. (c) Snapshot of phase separated states with and without passive forces at the same deformability and motility ($d = 0.1$, $Pe = 75$). Passive forces lead to a more spread-out spatial distribution of cells.

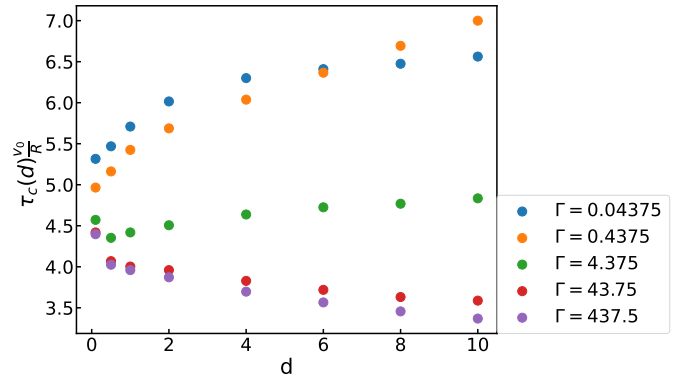


Fig. 6 Duration τ_c of a two-body collision as a function of deformability for different values of the substrate friction Γ . As the substrate friction is increased, the passive forces become less important than the self-propulsion velocity in determining the effective velocity v_i of a cell (see Eq. 3) and τ_c switches from increasing with deformability to decreasing with deformability.

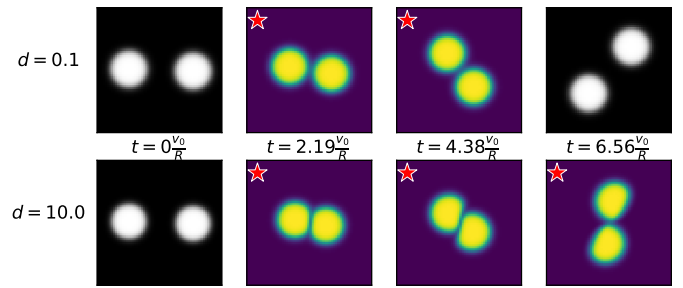


Fig. 7 Snapshots of two-body collisions. Frames in which the cells are not in contact are colored in black and white. When the cells are in contact, the frames are colored in purple and yellow and are also indicated by a star in the top left corner.

time unit is 64s, with a time step of $dt \sim 14$ ms and a total simulation time of ~ 35 hrs. As in previous work, we compute an auxiliary field $h(\vec{r}) = \sum_i^N \phi_i^2$, which allows us to solve for the individual phase field in parallel on their own subdomains^{28,31,32}. We choose a subdomain of size $L_{sub} \times L_{sub}$, where $L_{sub} = 35$, which is larger than a single cell but smaller than the whole system, with fixed boundary conditions ($\phi_i = 0$) on the boundary of the subdomain. As in previous work³², we keep the cell in the center of its subdomain by shifting its position when it has moved more than 2 lattice units in any direction, and we correspondingly update the position of the subdomain relative to the whole lattice. On the full simulation box, the boundary conditions are periodic. We initialize the system with cells that are placed randomly but non-overlapping, with a random initial velocity direction. On each sublattice, the field of the cell is initialized as a circle of radius R , with $\phi_i = 1$ inside the circle and $\phi_i = 0$ outside, centered at the center of the subdomain. We evolve the system without motility ($v_0 = 0$) for 10,000 time steps before turning on motility ($v_0 \neq 0$). This passive run allows the cells to develop a finite interface width and reach their equilibrium shape before turning on activity. We run the active simulations for 1.1×10^7 time steps on 12 processors, parallelized with OpenMP.

We have included videos of the system at $d=0.1$ and 10.0 with $Pe=75$ to show the system at various values of deformability

Acknowledgements

The work by A.H. and M.C.M. was supported by the National Science Foundation Grant No. DMR-2041459. This research has received funding (B. L.) from the European Research Council under the European Union's Horizon 2020 research and innovation programme (Grant Agreement No. 851196). Use was made of computational facilities purchased with funds from the National Science Foundation (CNS-1725797) and administered by the Center for Scientific Computing (CSC). The CSC is supported by the California NanoSystems Institute and the Materials Research Science and Engineering Center (MRSEC; NSF DMR 2308708) at UC Santa Barbara. This publication is funded in part by a grant from ICAM the Institute for Complex Adaptive Matter to A.H.

Notes and references

- 1 C. Bechinger, R. Di Leonardo, H. Löwen, C. Reichhardt, G. Volpe and G. Volpe, *Rev. Mod. Phys.*, 2016, **88**, 045006.
- 2 T. Vicsek, A. Czirók, E. Ben-Jacob, I. Cohen and O. Shochet, *Phys. Rev. Lett.*, 1995, **75**, 1226.
- 3 J. Toner and Y. Tu, *Phys. Rev. Lett.*, 1995, **75**, 4326.
- 4 H. Chaté, F. Ginelli, G. Grégoire and F. Raynaud, *Phys. Rev. E: Stat., Nonlinear, Soft Matter Phys.*, 2008, **77**, 046113.
- 5 A. Cavagna, I. Giardina and T. S. Grigera, *Phys. Rep.*, 2018, **728**, 1–62.
- 6 I. Buttinoni, J. Bialké, F. Kümmel, H. Löwen, C. Bechinger and T. Speck, *Phys. Rev. Lett.*, 2013, **110**, 238301.
- 7 X. Yang, M. L. Manning and M. C. Marchetti, *Soft Matter*, 2014, **10**, 6477–6484.
- 8 J. M. Belmonte, G. L. Thomas, L. G. Brunnet, R. M. de Almeida and H. Chaté, *Phys. Rev. Lett.*, 2008, **100**, 248702.
- 9 E. Méhes, E. Mones, V. Nemeth and T. Vicsek, *PLoS One*, 2012, **7**, e31711.
- 10 S. R. McCandlish, A. Baskaran and M. F. Hagan, *Soft Matter*, 2012, **8**, 2527–2534.
- 11 J. Tailleur and M. Cates, *Phys. Rev. Lett.*, 2008, **100**, 218103.
- 12 Y. Fily and M. C. Marchetti, *Phys. Rev. Lett.*, 2012, **108**, 235702.
- 13 F. Farrell, M. Marchetti, D. Marenduzzo and J. Tailleur, *Phys. Rev. Lett.*, 2012, **108**, 248101.
- 14 J. Bialké, H. Löwen and T. Speck, *EPL*, 2013, **103**, 30008.
- 15 J. Stenhammar, A. Tiribocchi, R. J. Allen, D. Marenduzzo and M. E. Cates, *Phys. Rev. Lett.*, 2013, **111**, 145702.
- 16 Y. Fily, S. Henkes and M. C. Marchetti, *Soft Matter*, 2014, **10**, 2132.
- 17 J. Stenhammar, D. Marenduzzo, R. J. Allen and M. E. Cates, *Soft Matter*, 2014, **10**, 1489.
- 18 M. E. Cates and J. Tailleur, *Annu. Rev. Condens. Matter Phys.*, 2015, **6**, 219–244.
- 19 G. S. Redner, M. F. Hagan and A. Baskaran, *Phys. Rev. Lett.*, 2013, **110**, 055701.
- 20 T. F. Farage, P. Krinninger and J. M. Brader, *Phys. Rev. E: Stat., Nonlinear, Soft Matter Phys.*, 2015, **91**, 042310.
- 21 P. Digregorio, D. Levis, A. Suma, L. F. Cugliandolo, G. Gonnella and I. Pagonabarraga, *Phys. Rev. Lett.*, 2018, **121**, 098003.
- 22 M. Paoluzzi, D. Levis and I. Pagonabarraga, *Commun. Phys.*, 2022, **5**, 111.
- 23 R. Großmann, I. S. Aranson and F. Peruani, *Nat. Commun.*, 2020, **11**, 5365.
- 24 P. Nie, J. Chattoraj, A. Piscitelli, P. Doyle, R. Ni and M. P. Ciamarra, *Phys. Rev. Res.*, 2020, **2**, 023010.
- 25 M. Sanoria, R. Chelakkot and A. Nandi, *Phys. Rev. E*, 2021, **103**, 052605.
- 26 M. Sanoria, R. Chelakkot and A. Nandi, *Phys. Rev. E*, 2022, **106**, 034605.
- 27 N. Lauersdorf, T. Kolb, M. Moradi, E. Nazockdast and D. Klotsa, *Soft Matter*, 2021, **17**, 6337–6351.
- 28 M. Nonomura, *PloS one*, 2012, **7**, e33501.
- 29 J. Löber, F. Ziebert and I. S. Aranson, *Sci. Rep.*, 2015, **5**, 9172.
- 30 B. Palmieri, Y. Bresler, D. Wirtz and M. Grant, *Sci. Rep.*, 2015, **5**, 11745.
- 31 R. Mueller, J. M. Yeomans and A. Doostmohammadi, *Phys. Rev. Lett.*, 2019, **122**, 048004.
- 32 B. Loewe, M. Chiang, D. Marenduzzo and M. C. Marchetti, *Phys. Rev. Lett.*, 2020, **125**, 038003.
- 33 G. Zhang, R. Mueller, A. Doostmohammadi and J. M. Yeomans, *J. R. Soc., Interface*, 2020, **17**, 20200312.
- 34 L. Balasubramaniam, A. Doostmohammadi, T. B. Saw, G. H. N. S. Narayana, R. Mueller, T. Dang, M. Thomas, S. Gupta, S. Sonam, A. S. Yap *et al.*, *Nat. Mater.*, 2021, **20**, 1156–1166.
- 35 A. Hopkins, M. Chiang, B. Loewe, D. Marenduzzo and M. C. Marchetti, *Phys. Rev. Lett.*, 2022, **129**, 148101.
- 36 C. Ritter, N. Lejnse, Y. Farhangi Barooji, J. M. Brickman, A. Doostmohammadi and L. B. Oddershede, *arXiv*, 2022, preprint, arXiv:2209.09707, <https://arxiv.org/abs/2209.09707>.
- 37 J.-M. Armengol-Collado, L. N. Carenza, J. Eckert, D. Krommydas and L. Giomi, *arXiv*, 2022, preprint, arXiv:2202.00668, <https://arxiv.org/abs/2202.00668>.
- 38 M. E. Cates and E. Tjhung, *Journal of Fluid Mechanics*, 2018, **836**, P1.
- 39 R. A. Foty and M. S. Steinberg, *Developmental biology*, 2005, **278**, 255–263.
- 40 B. Liebchen, D. Marenduzzo and M. E. Cates, *Physical review letters*, 2017, **118**, 268001.
- 41 H. Zhao, A. Košmrlj and S. S. Datta, *arXiv*, 2023, preprint arXiv:2301.12345, <https://arxiv.org/abs/2301.12345>.
- 42 M. Chiang, A. Hopkins, B. Loewe, D. Marenduzzo and M. C. Marchetti, *in preparation*.